BAMS Article

The Bioaerosols and Convective Storms (BACS) Field Campaigns: Variability in Cold Pool Characteristics and Aerosol Responses

R. J. Perkins,[a] B. Ascher,[a,g] T. W. Barbero,[a] N. Bryan,[a,f] C. M. Davis,[a] P. J. DeMott,[a] J. Escobedo,[a] N. M. Falk,[a] J. C. Fernando,[b] T. K. Feldman,[b] S. W. Freeman,[c,d] B. Heffernan,[a] T. C. J. Hill,[a] D. Juergensen,[a] S. M. Kreidenweis,[a] G. Leung,[a,h] C. B. A. Mampage,[b] A. C. Mazurek,[a] C. Mignani,[a,e] C. A. Neumaier,[a] M. Nieto-Caballero,[a] E. A. Sherman,[a] S. C. van den Heever,[a] D. Veloso-Aguila,[a] L. D. Grant,[a] and E. A. Stone[b]

KEYWORDS: Aerosol-cloud interaction; Aerosols/particulates; Biosphere/atmosphere interactions; Cold pools; Convective storms; Field experiments

ABSTRACT: Bioaerosols have important impacts on human health and potentially on weather and climate through aerosol–cloud interactions. Reciprocally, weather systems can have a large impact on bioaerosols both indirectly through ecosystem-level influences and by playing a more direct role in bioaerosol emission, deposition, and transport. In this work, we discuss the design and initial findings of the Bioaerosols and Convective Storms (BACS) field campaigns, a project targeting the interplay of these two effects. Two BACS field campaigns were conducted in the springs of 2022 and 2023, examining the dynamics of speciated and cloud-relevant aerosol and, especially, bioaerosol observations surrounding precipitation events and cold pool outflows from convective storms. A multifaceted deployment strategy was used, leveraging a combination of online and offline measurements of aerosol and bioaerosol distributions, cloud-relevant properties, and chemical tracers in the context of atmospheric state measurements. The observational strategy included measurements at ground level, a 9-m flux tower, and simultaneous stacked column and profiling multirotor drone measurements and radiosonde launches. Aerosol and bioaerosol responses to precipitation and cold pool events are examined within this manuscript through several case studies highlighting that similar events can produce very different aerosol responses. Reasons for this variability are hypothesized and discussed in the context of our campaign data, and targets for future investigations are suggested.

SIGNIFICANCE STATEMENT: This work is motivated by understanding a phenomenon with direct human impacts; storm lofting and transport of bioaerosols are known to cause health impacts such as "thunderstorm asthma," while the same sources of bioaerosols may additionally impact storm evolution. This work describes an extensive campaign dataset, showcasing two cases to highlight how the dataset can be used to probe these questions and raising some of the crucial scientific questions requiring further investigation.

DOI: 10.1175/BAMS-D-25-0105.1

Corresponding author: Russell Perkins, rperkins@colostate.edu

Supplemental information related to this paper is available at the Journals Online website: https://doi.org/10.1175/BAMS-D-25-0105.s1.

Manuscript received 10 April 2025, in final form 8 April 2026, accepted 17 April 2026

AFFILIATIONS: [a] Department of Atmospheric Science, Colorado State University, Fort Collins, Colorado; [b] Department of Chemistry, The University of Iowa, Iowa City, Iowa; [c] Department of Atmospheric and Earth Science, University of Alabama in Huntsville, Huntsville, Alabama; [d] Earth System Science Center, University of Alabama in Huntsville, Huntsville, Alabama; [e] Water and Soil Resource Research, Institute of Geography, University of Augsburg, Augsburg, Germany; [f] Mass General Brigham, Boston, Massachusetts; [g] Meteorological Institute Munich, Ludwig Maximilian University of Munich, Munich, Germany; [h] Department of Atmospheric and Oceanic Sciences, University of Wisconsin–Madison, Madison, Wisconsin

1. Introduction

Biological materials in Earth's atmosphere have been increasingly recognized for their importance in human health and interactions with clouds. Exchange of biological materials between Earth's surface and atmosphere is known to occur but remains challenging to characterize due partly to the episodic and circumstantial nature of bioaerosol release. The purpose of this study is to improve understanding of the mechanisms and magnitudes of this exchange, particularly in association with convective storm processes, as well as important impacts on cloud systems.

Primary biological aerosol particles, simply bioaerosols hereafter, are directly emitted biological materials suspended in the air. Bioaerosols exist as a wide range of materials spanning the entire aerosol size range (Fröhlich-Nowoisky et al. 2016), and biological materials can be internally mixed with other aerosol materials, which can lead to large differences in reported bioaerosol abundances (Jaenicke 2005; Zawadowicz et al. 2019), requiring clarity about how the term bioaerosol is used. Aerosols and bioaerosols can also be emitted through raindrop impaction (Hirst and Stedman 1963; Joung et al. 2017; Mignani et al. 2025), while bioaerosol release can be more specifically influenced by changes in moisture, such as associated with convective storm systems, thus triggering active fungal spore emission (Elbert et al. 2007; Janssen et al. 2021) and pollen rupture (Suphioglu et al. 1992; Taylor et al. 2002). Pollen grain rupture into subpollen particles has been associated with severe convective storms like squall lines, leading to widespread health impacts such as asthma attacks in a phenomenon termed "thunderstorm asthma" (D'Amato et al. 2016; Harun et al. 2019). Cloud phase and properties can be influenced by bioaerosols through action as cloud condensation nuclei (CCN) and ice nucleating particles (INPs), discussed below. There is strong evidence that internally mixed bioaerosols have cloud-relevant properties similar to pure bioaerosols (Conen et al. 2011; Fröhlich-Nowoisky et al. 2015; O'Sullivan et al. 2016; Augustin-Bauditz et al. 2016). Given this support of internally mixed biological particles, for example, a mineral dust particle attached to a cell fragment or cell-free protein, maintaining bioaerosol-specific properties, we define them as bioaerosols as well. Materials such as biomass burning aerosols (smoke) and secondary aerosols derived from gas-phase biological emissions are excluded. Bioaerosols can be a significant fraction of supermicron aerosol number and mass in a wide range of environments (Fröhlich-Nowoisky et al. 2016).

Convective storms can influence emission, deposition, and transport of bioaerosols through a variety of pathways, but the magnitude of these effects is often unknown or difficult to predict. Wet deposition can remove aerosols through scavenging either in-cloud or below cloud by falling precipitation (Duce et al. 1991; Cheng et al. 2021). Evaporation of rain and melting of ice hydrometeors produced by storms cool the surrounding air and form downdrafts, which

sink and then spread out along the surface as cold pools. Cold pools propagate as density currents (Benjamin 1968; Falk et al. 2025) and are typically cooler and gustier than their surroundings (Charba 1974; Engerer et al. 2008; van den Heever et al. 2021). Their passage can, therefore, be detected by changes in temperature and winds (Engerer et al. 2008; Provod et al. 2016). Cold pools are critical for initiating storms by mechanically lifting air that can ultimately comprise an updraft (Purdom 1976; Droegemeier and Wilhelmson 1985a) and by cold pool collisions (Droegemeier and Wilhelmson 1985a,b; Meyer and Haerter 2020; Falk and van den Heever 2023). Cold pools also play important roles in determining the structure and propagation of organized storm systems such as squall lines (Thorpe et al. 1982; Rotunno et al. 1988; Weisman and Rotunno 2004). Cold pool wind action at the surface can loft aerosols such as dust (Miller et al. 2008; Seigel and van den Heever 2012; Bukowski and van den Heever 2022) and bioaerosols. These cold-pool-lofted aerosols can potentially be ingested into the parent or subsequent storms. Seigel and van den Heever (2012) found that dust lofted within a supercell cold pool can be ingested in small quantities into its parent storm updraft through mixing across the cold pool's leading edge, although larger quantities were ingested when the dust was present in the supercell storm's environment or in the presence of interacting cold pools. Grant et al. (2018) also found that cold pool air was transported into tropical oceanic convective storm updrafts and only recently have the specific mechanisms for this lofting and the sensitivity of these findings to storm morphology or environment been studied (Davis et al. 2025). Downdrafts associated with cold pools and their parent convection can also impact near-surface aerosol concentrations by entraining air from the free troposphere (Dickerson et al. 1987), which often, but not always, contains lower concentrations of aerosols than the boundary layer.

Bioaerosols likely influence cloud phase. Deep convective storms extend from the relatively warm boundary layer to the upper troposphere where temperatures are well below the homogeneous freezing level (–38°C), where liquid water will freeze spontaneously. Cloud phase has important impacts on cloud lifetime, precipitation, and radiative properties, with ultimate impacts on local, regional, and global-scale climate and weather (Lohmann and Neubauer 2018; Morrison et al. 2020; Hofer et al. 2024). Therefore, it is essential to consider the ice-phase microphysical properties of deep convection, as well as whether bioaerosols, if transported into convective updrafts, can impact this ice formation within the storm's mixed-phase region. Freezing at temperatures warmer than –38°C requires interaction with an INP (primary nucleation) or contact with an existing ice crystal (secondary nucleation). Primary nucleation can occur through several pathways, but immersion freezing, where the INP is immersed within a cloud droplet, is considered to be the most relevant process in cloud regions warmer than –38°C (Hoose and Möhler 2012; Kanji et al. 2017). Concentrations of INPs are temperature dependent, with INPs capable of initiating freezing often increasing exponentially as temperatures decrease. In contrast, secondary nucleation or secondary ice production (SIP) occurs through contact with an existing ice crystal, often considered to be produced through fragmentation or splintering processes (Field et al. 2017; Korolev and Leisner 2020). Because SIP processes depend on initial freezing events, an understanding of primary nucleation is critical to accurately characterizing and representing SIP within models. An understanding of concentrations of INPs active at warm temperatures, > –15°C, may be particularly important due to coincidence with the temperature range most favorable to SIP. Biological materials have been observed to constitute a large portion of the INPs within this temperature range in many environmental contexts (Suski et al. 2018; Testa et al. 2021; Pereira Freitas et al. 2023). Bioaerosols could, therefore, alter convective microphysical properties, which has been investigated for pollen and pollen fragments in a few recent numerical modeling studies (Wozniak et al. 2018; Werchner et al. 2022; Subba et al. 2023), but remains underexplored for other bioaerosol types.

Bioaerosol and cloud systems are coupled: Precipitation and cold pools can impact bioaerosol concentrations through emission, transport, and deposition mechanisms, while bioaerosols can alter cloud phase and precipitation. This raises the possibility of important feedbacks existing in these systems. For example, it is plausible that a precipitating storm could prompt the release of biological INPs, which could be ingested into the parent storm or a subsequent storm in the region, altering the cloud phase and intensifying precipitation, leading to further bioaerosol release. These changes could occur on relatively short time scales in localized regions associated with storm-scale processes, which would not be well captured by long-term measurement strategies, such as offline aerosol samples collected over many hours, often used to characterize INP concentrations. Past measurements have found strong relationships between bioaerosol or INP concentrations and sampling periods influenced by rainfall, but analysis has been on longer time scales where the details of any coupling are unclear (Huffman et al. 2013; Yue et al. 2016; Gosselin et al. 2016; Hughes et al. 2020). The Bioaerosols and Convective Storms (BACS) campaign was designed to probe both these shorter and longer time scales and to assess the importance of these feedbacks by probing the individual mechanisms related to the interactions of convective storms and bioaerosols through the investigation of bioaerosol identities, INP properties, emission, deposition, and transport by and within and surrounding convective events.

2. Field campaign overview

The BACS field campaigns took place in two phases, in the springs of 2022 and 2023 at the Central Plains Experimental Range (CPER) site in the northern Colorado plains, operated by the U.S. Department of Agriculture's Agricultural Research Service. The site is a 62.9 km^2 semiarid grassland site that is well characterized and use controlled (Hazlett 1998; Steinert 2016; Krauss et al. 2018) and utilized for cattle grazing studies (Augustine et al. 2024), among other research activities. The very broad (>100 000 km^2) surrounding region is utilized as ~35% cropland and ~60% rangeland managed for livestock production (Augustine et al. 2021; Augustine et al. 2024). While the land use of the CPER site is more tightly controlled than the surrounding region, it is still regionally representative.

The first field campaign, BACS-I, took place from 23 May through 18 June 2022, while BACS-II took place from 22 May through 23 June 2023. Within the CPER site, operations were held at two sublocations. A full list of instrumentation, offline analyses, and deployment locations for BACS-I and BACS-II are available in Table S1 in the online supplemental material, while a schematic of the sampling locations and measurements at each site is shown in Fig. 1. The first measurement location was the National Science Foundation (NSF) National Ecological Observatory Network (NEON) location within CPER at 40.8155°N, 104.7456°W. At this location, henceforth referred to as the tower site, instrumentation was placed at the 9-m tower top, in the CSU mobile laboratory that was parked across from the NEON instrument shed at the tower base, and within the fenced enclosure of soil plot 3 [~300-ft northwest (NW) of the tower] but outside of the central measurement area of the enclosure. Instrumentation at the tower location was generally focused on aerosol characterization measurements. Aerosol and rainwater samples collected at soil plot 3 provided more in-depth chemical and biological analyses, including endotoxin, carbohydrates, inorganic ions, and deoxyribonucleic acids (DNA). The second measurement location was at the Semi-Arid Grasslands Research Center (SGRC), a Colorado State University–USDA partnership site located at 40.8095°N, 104.7778°W. This site supported airborne measurements through multirotor drone flights and radiosonde releases, as well as aerosol and precipitation characterization. The NEON tower site is approximately 1.7 miles east of the SGRC site, sometimes resulting in a temporal delay between mesoscale events affecting measurements at the two sites,

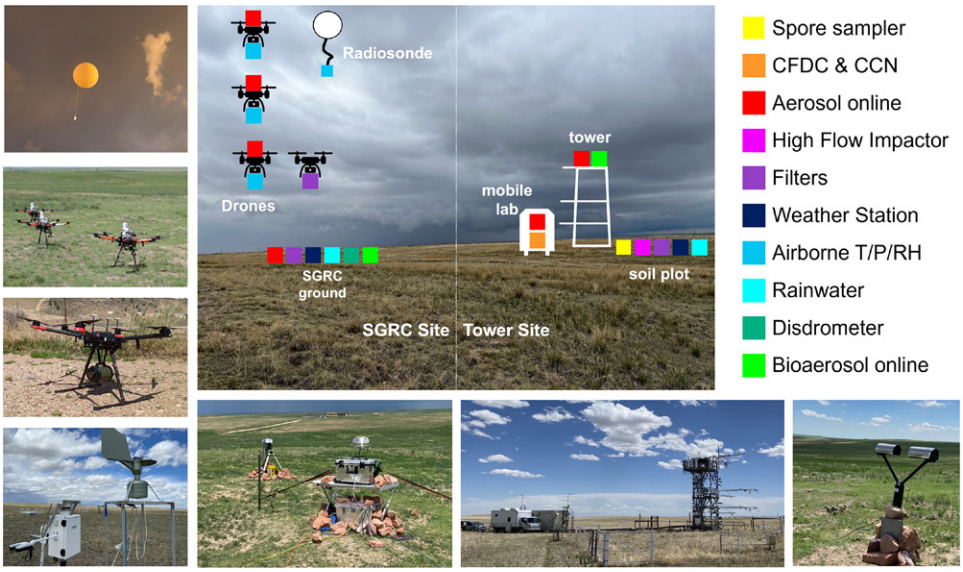

Fig. 1. Overview of the BACS instrumentation within the CPER site, Colorado. Schematic of the two measurement sites (SGRC and tower), along with pictures of select instrumentation. (from top left, counterclockwise) A launched radiosonde, drones outfitted for thermodynamic and aerosol measurements, a drone with attached filter sampling system, rainwater and pollen/spore samplers, SGRC aerosol instruments and filter samplers, NEON tower with soil plots and mobile laboratory, and disdrometer instrument.

depending on the direction from which the event originated and the speed at which the storm systems of interest were moving.

Additionally, complementary data were collected through collocated and collaborative field campaigns by the NSF-sponsored Biology Integration Institute: Regional OneHealth Aerobiome Discovery Network (BROADN). BROADN activities at the CPER site overlapped with the BACS campaigns, with some additional BROADN activities continuing into other seasons. BROADN measurements during the 2023 BACS field campaign included complementary 12-h (day and night) DNA and INP air-filter-based measurements at the NEON tower top and base and SGRC site, as well as INP sampling focused around rainfall events (Mignani et al. 2025).

Twenty-eight intensive observation periods (IOPs), 14 each during BACS-I and BACS-II, were targeted around forecasted atmospheric conditions that were likely to produce convective storms. Motivated by their bioaerosol transport and lofting capabilities, cold pools were specifically targeted in this study, and more than 50 cold pools were observed across the 28 IOPs. The sampling strategy for these IOPs targeted drone flights and sounding measurements before, during, and after cold pool passages. Ideally, drone flights would start before passage and continue well into the cold pool, but sometimes high wind conditions, rainfall, or other severe weather hazards required that drones be grounded for safety.

The BACS-I and BACS-II field campaign periods contrasted markedly in precipitation and prevailing flow regimes. Rank maps for precipitation are shown for the PRISM (PRISM Group 2023; Daly et al. 2000) data products in Fig. 2, alongside representative images of vegetation. In the 44-yr PRISM dataset, conditions at the site for BACS-I were in the 15th driest, while in BACS-II, they were in the record fifth wettest, with more extreme dry and wet conditions for each year, respectively, in the surrounding region. Precipitation measurements collected during these field campaigns are in line with these extreme conditions, with 10.1 mm of precipitation falling in the 27-day period of BACS-I contrasted by 118.5 mm of precipitation received in the 33-day BACS-II period (Fernando et al. 2025).

The contrasting meteorology led to visible changes in the vegetation across the two study periods as well, with more abundant and greener vegetation in BACS-II (Fig. 2). The area

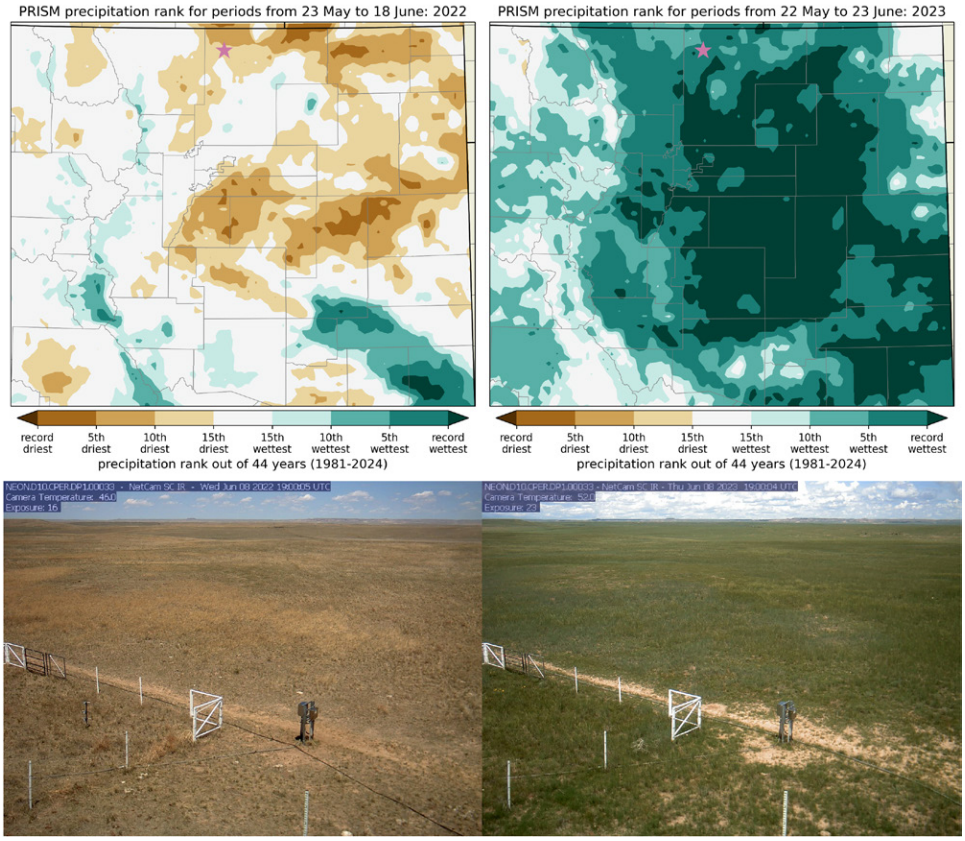

Fig. 2. (top) PRISM precipitation rank maps for the NW ~2/3 of Colorado during the time periods of (left) BACS-I and (right) BACS-II field campaigns, showing approximately 38°–41°N and 102°–107°W. The campaign location is denoted by a red star. County lines and state lines are denoted by gray and black lines, respectively. (bottom) NEON phenology images (NEON 2025a) at 1200 LT 8 Jun for (left) BACS-I and (right) BACS-II. The BACS-I image was taken at lower exposure, and a 44% increased exposure has been applied for better comparison with the BACS-II image.

between the SGRC and tower measurement sites even developed a small pond that persisted over the BACS-II campaign that was not present during BACS-I. These changes in precipitation and vegetation certainly had cascading impacts on the ecosystem down to the microbial level, which can be investigated using our dataset alongside products collected through NEON and BROADN.

3. Key findings

One of the most prominent findings of the BACS field campaigns is the high degree of variability observed in the cold pool characteristics (Falk et al. 2025) and the responses of aerosols and bioaerosols to these cold pool passage events (Feldman et al. 2026). Observed cold pools were produced by deep convection ranging from isolated storms to squall lines and other frontal systems. Their properties were highly variable, as shown in Fig. 3, which summarizes all cold pools detected on IOP dates from the surface station deployed at the SGRC site. Cold pools were slightly colder but less windy in BACS-II compared to BACS-I, although BACS-I cold pools had more outliers in the magnitude of the change in virtual potential temperature ($\Delta\theta_v$) and wind vector ($\mathbf{\Delta U}$) as well as the strongest cold pool observed throughout the campaign in association with a squall line. Cold pools were also slightly drier in BACS-II than in BACS-I (Fig. 3). Cold pool θ_v and wind vector perturbations spanned one to two orders of magnitude. Most cold pools also exhibited both a dry and moist perturbation at some point within the hour after initial cold pool passage, since maximum (minimum) water vapor perturbations (Δr_v) were typically positive (negative) (Fig. 3). The high degree

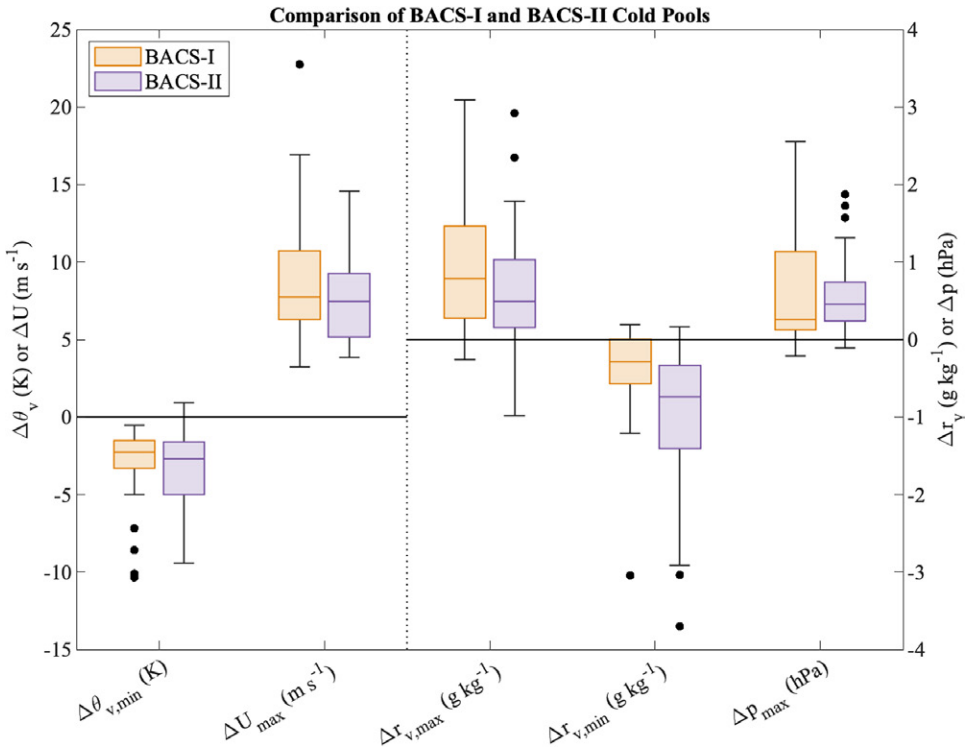

FIG. 3. Box-and-whisker plots of CP properties from the SGRC surface station measurements on all IOP dates: virtual potential temperature and wind vector (left ordinate), water vapor mixing ratio, and pressure (right ordinate). CP initial passage was first determined from radar imagery and field notes and refined based on the timing of first decrease in temperature, increase in wind speed, or change in wind direction, whichever occurred earliest. Maximum or minimum perturbations (denoted as Δ) are calculated within 1 h after CP passage or until the passage of an additional CP, whichever occurred earlier, relative to 15-min averages before the initial CP passage. The ΔU represents the magnitude of the vector change in horizontal wind. Note that identified CPs include those outside of the IOP time period if they occurred on the same day but do not include non-IOP dates. The 27 (40) CPs were detected during BACS-I (BACS-II) IOP dates.

of cold pool variability was the case for events observed in a single year and was not solely due to yearly changes in rainfall and vegetation.

To highlight this variability and factors that should be considered in future work, while showcasing the synergistic measurement approach and interesting features within the BACS datasets, we discuss two case studies. The first is IOP22, which occurred on 8 June 2023, during the BACS-II deployment. This case includes a cold pool from the west (CP1), a period of rainfall at the site accumulating 2.76 mm, and an additional cold pool from the north (CP2) over the course of ~1.5 h (Figs. 4a,c and 5a–c). The second case we consider, IOP06 (3 June 2022) during the drier BACS-I deployment, was chosen for its nominal similarities in cold pool and precipitation events to IOP22 but contrasting aerosol responses to cold pools and precipitation. The first cold pool event (hereafter referred to as CP3, to distinguish from the IOP22 cold pools) included collision of a boundary from the southwest and another cold pool from the north, followed by a period of light precipitation and an additional cold pool from the west (CP4) in a similar ~1.5-h time frame (Figs. 4b,d and 5d–f). An overview of the meteorological and aerosol conditions from both case study example periods is shown in Fig. 4, with radar images and annotated cold pool (black arrows for CP1/CP3, pink arrows for CP2/CP4) and precipitation features (red arrows) shown in Fig. 5 and radiosonde and drone profiling data shown in Fig. 6. Both of these events are cold pool train events (Neumaier 2023; Neumaier et al. 2026, manuscript submitted to *J. Atmos. Sci.*) in that more than one cold pool passes over the same site on the same day without colliding.

Cold pool identification and passage times are determined from a combination of changes in surface temperature and wind data (Figs. 4a–d), aided by radar reflectivity data (Fig. 5) which often shows the leading edge of the cold pool as an arc or line of enhanced radar returns caused by convergence and lofting of debris by the cold pool's head circulation (Markowski and Richardson 2010). Sounding data (Fig. 6) are additionally used to assess cold pool thermodynamic profiles and depths and to confirm suspected passage events from other data. These different data streams do not always agree in their indication of the cold pool characteristics and passage times, however. The uncertainty in passage times subsequently creates uncertainty in how measured variables change with cold pool passage. Here, passage windows are defined broadly to capture this uncertainty.

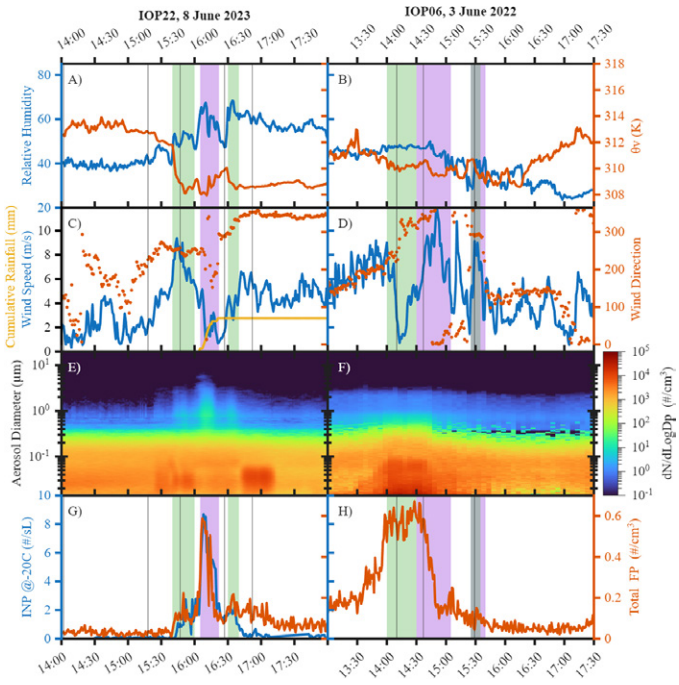

Fig. 4. Evolution of key measurements at the NEON tower site for (left) IOP22 and (right) IOP06 periods, with all times in local (UTC – 6 h). CP passage times are shown with green fill, while periods of precipitation are shown with purple fill, with overlapping times appearing gray. Radiosonde launch times are shown with thin black vertical lines, with corresponding sonde data presented in Fig. 6. (a),(b) Relative humidity (%) (blue, left axis) and virtual potential temperature (K) (orange, right axis). (c),(d) Wind speed (m s^{-1}) and cumulative rainfall (mm) (blue and yellow, respectively, left axis) and wind direction (°) (orange, right axis). Very light precipitation in IOP06 consisted of several periods of drizzle/light rain and virga within the shaded region, with no measurable precipitation accumulation at the tower site. (e),(f) Aerosol size distribution, with colors mapped to the scale bar on the right. (g),(h) INP concentration (number/sL) for particles smaller than 2.5 μm measured at –20°C and 5% water supersaturation [left, blue, (g) only] and total FPs > ~500 nm (number/cm³) (orange, right). Temperature, pressure, and wind data are obtained from the NEON bundled Eddy Covariance system (NEON 2025b).

Cold pool properties can be estimated relative to their environments through measured differences in temperature, buoyancy, humidity, or winds, but different values can be obtained depending on the location measured within the cold pool relative to its leading edge and the method of calculation used (Grant et al. 2024; Falk et al. 2025). Here, we use wind speed and direction, depth, and virtual potential temperature, as a measure of buoyancy, calculated using the simplified/approximate form (Markowski and Richardson 2010):

$$\theta_v = \theta\left(1+0.61r_v\right) = T\left(\frac{P_0}{P}\right)^{0.286}\left(1+0.61r_v\right),$$

where θ is the potential temperature, r_v is the water vapor mixing ratio, P is the pressure, P_0 is the reference pressure, and the rightmost equation has been expanded for θ.

To build accurate relationships between cold pool properties and aerosol responses, the variations in how cold pools can be characterized must be considered. Changes over time due to a cold pool passage can be convoluted with changes outside the cold pool in both thermodynamic and aerosol variables resulting from previous cold pools, radiative heating of the surface, latent and sensible heat fluxes, or other factors. To mitigate this, it is important to consider precold pool measurements as close to the beginning of the cold pool passage window

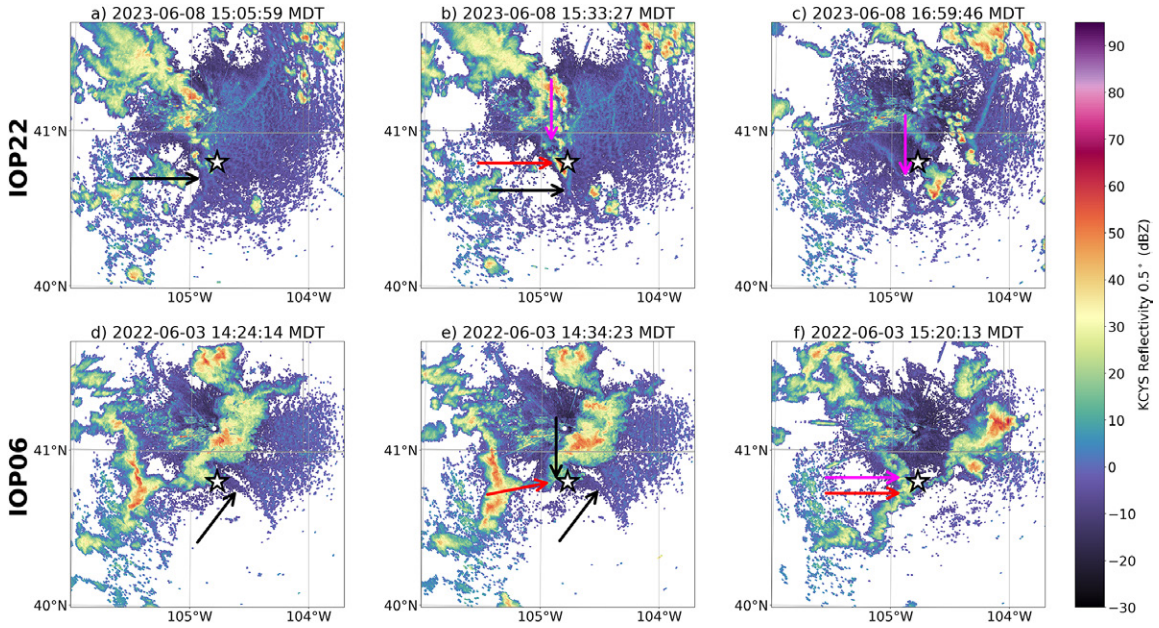

Fig. 5. Radar reflectivity from KCYS NEXRAD Doppler radar in Cheyenne, WY (white dot), located to the north of the field site (white star), at key times surrounding rainfall and storm evolution from (a)–(c) IOP22 and (d)–(f) IOP06. The first CP events of each IOP are annotated with black arrows [(a),(b) CP1, (d),(e) CP3], second CP events with pink arrows [(b),(c) CP2, (f) CP4], and precipitation events with red arrows in (b), (e), and (f).

as possible, which was an important consideration of our IOP measurement strategies. While sounding data are available generally within the broadly defined passage window, sounding launches do not always occur in the strongest portion of the cold pool, and cold pools are often but not always coldest at the surface [especially under scenarios with strong surface fluxes, e.g., Grant and van den Heever (2016, 2018), and both IOPs shown in Fig. 6]. These complexities highlight the need for multiple measurement strategies in accurately assessing cold pool properties, as was done during BACS. The drone thermodynamic measurements performed for this campaign were designed to bridge the vertical resolution of the sounding measurements and the temporal resolution of surface measurements. An example of the fine-scale temporal evolution around IOP22 CP2's passage obtained from the vertically profiling drone is shown in Figs. 6c and 6d. It is clear that while the drone profile measurements broadly agree with the radiosonde data, the high (2 min) resolution in profile data captures variations such as the passage of the deeper cold pool head (Fig. 6c at 1638–1640 LT) and undulations in the depth farther back in the cold pool (Fig. 6d), allowing for study of the relationship between this fine-scale evolution and other changes such as in the aerosol properties. Estimates of cold pool properties from surface, radiosonde, and drone data are shown in Table 1. CP1 has the largest thermodynamic perturbation and is also the deepest cold pool among the four, while CP3 is thermodynamically the weakest. However, CP2 and CP4 are the shallowest, while CP4 is associated with the largest increase in wind speed. Within the broader context of all cold pool measurements from their associated campaign years (Fig. 3), none of these cold pools are uncommonly strong or weak in their surface characteristics, though CP3 is in the lower 25th percentile for $\Delta\theta_v$.

Cold pools and rainfall events might impact aerosol concentrations through a number of mechanisms that depend on the properties of these events, such as emission by raindrop impaction and cold pool winds, removal through in-cloud and below-cloud scavenging, moisture-induced bioaerosol release and pollen rupturing, and transport of cloud-processed and free tropospheric air by downdrafts. IOP22 had a single rainfall period accumulating 2.76 mm with cold pool passage events before and after. During this rainfall period, comparing

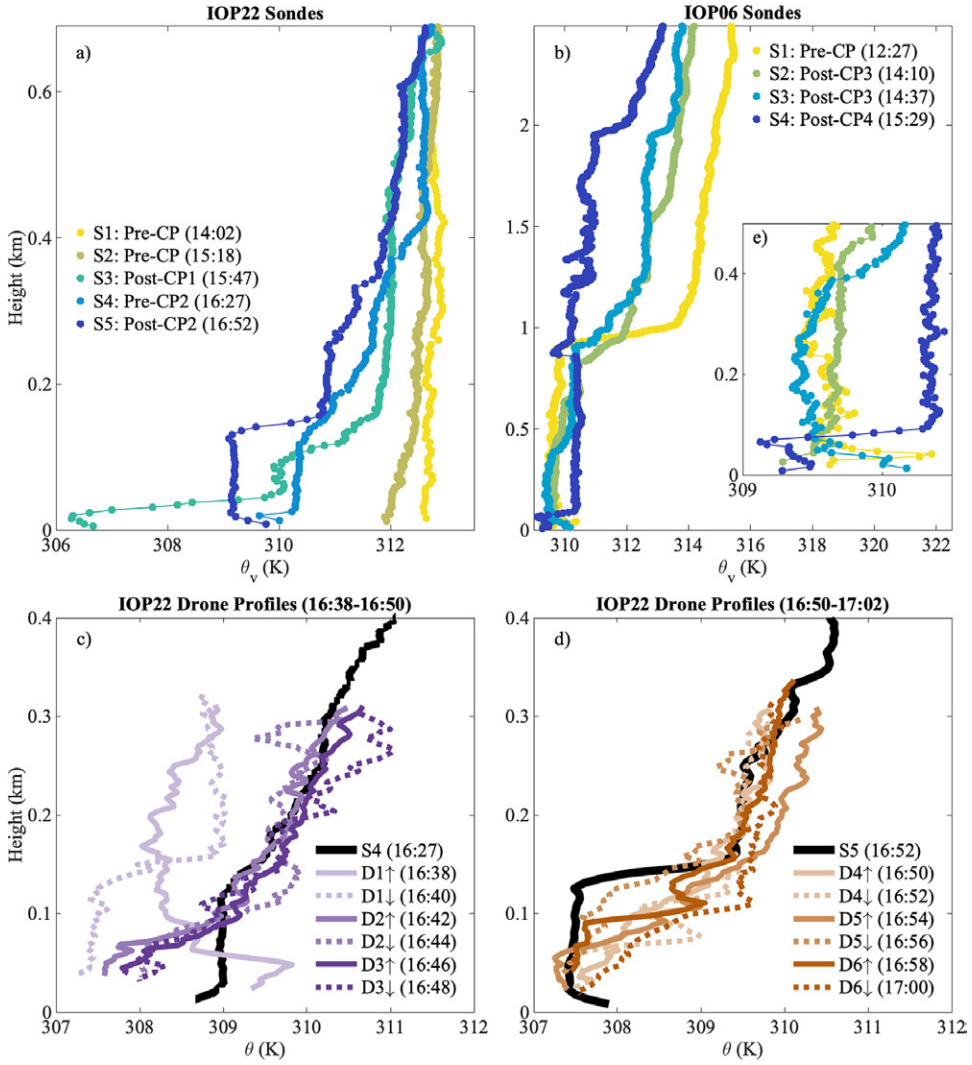

Fig. 6. Thermodynamic profiles collected from radiosondes during (a) IOP22 and (b),(e) IOP06, depicting virtual potential temperature (K) as a function of height (km AGL). Note the different vertical axis scaling between (a), (b), and (e). Panel (e) is the zoomed inset within panel (c) showing the CP structure near the surface. (c),(d) Ascending and descending potential temperature profiles collected from the profiling drone around CP2 passage during IOP22. Profiles 1–3 are shown in (c), starting 11 min after S4 (pre-CP2 radiosonde) was launched, while profiles 4–6 are shown in (d), around the S5 (post-CP2) radiosonde launch.

Table 1. Measured CP properties. Data are obtained from the tower, radiosonde launches, and for CP2, drone profiles. Depth is estimated from radiosondes as the lowest altitude where θ_v (buoyancy) in the CP sonde matches the pre-CP value or as the height of the strongest stable layer from drone profiles. Ranges are provided where two events interact (CP3) or where multiple data sources are used (CP2 depth). The Δ_{max} surface quantities are calculated as the largest change between immediately pre- to post-CP passage.

	IOP22		IOP06	
	CP1	CP2	CP3	CP4
$\Delta\theta_v$ surface	–3.7 K	–1.6 K	–0.8 K	–1.5 K
$\Delta\theta_v$ sonde	–5.6 K	–1.2 K	–0.3 K	–1.0 K
Δv surface	4 m s^{-1}	3 m s^{-1}	–6.5 then 4.5 m s^{-1}	7.5 m s^{-1}
$\lvert\Delta w_{dir}\rvert$ surface	0°	35°	20° then 60°	75°
Depth	600 m	75–350 m	400 m	75 m
Direction propagating from	W	N	SW then N	W

pre-CP to peak concentrations, there was a ~20× increase in concentrations of particles with diameters > 500 nm; a > 16× increase in fluorescent particle (FP) concentrations, used as a proxy for bioaerosols; and a >40× increase in INP concentrations (Figs. 4e,g). IOP06 had two light-precipitation periods, with intermittent light rain/drizzle and virga and with no precipitation accumulation at the tower or SGRC locations as indicated by the rainwater sampler and rainwater sensors. The second precipitation period coincided with a cold pool passage event. Multi-Radar Multi-Sensor (MRMS) system radar precipitation products (Zhang et al. 2016) show no rainfall, but field notes confirm rainfall at SGRC in this period (Grant et al. 2026). Aerosol responses contrasting those for IOP22 are observed in IOP06, with aerosol and fluorescent particle concentrations starting enhanced prior to precipitation, decreasing > 5× over the course of the first precipitation event, and remaining unperturbed during the second precipitation/cold pool passage period (Figs. 4f,h) (no online INP measurements were available for IOP06). The changes in precipitation intensity between IOP22 and IOP06, possibly modulated by the seasonal differences between the two campaign years (Fig. 2), seem the most probable explanation for the different aerosol responses, with more intense precipitation in IOP22 associated with higher aerosol emissions and thus concentrations. For IOP06, the removal and/or dilution (by clean free-tropospheric air) processes dominate generation for the first precipitation event but approximately balance one another for the second precipitation period. The changes observed in fluorescent particle concentrations and INP concentrations with rainfall are within the same order of magnitude captured by previous studies (Huffman et al. 2013; Yue et al. 2016; Hughes et al. 2020; Gosselin et al. 2016). Different biological materials seem likely to be important in different ecological settings, with measurements from Gosselin et al. (2016), Huffman et al. (2013), and Yue et al. (2016) supporting emission of fungal spores and bacteria, while Hughes et al. (2020) found evidence of pollen rupture dominating bioaerosol concentration changes.

Cold pool impacts on aerosol properties likely depend at least partly on the rainfall impacts on aerosols, discussed above. Aerosol changes in regions of rainfall will often occur within a cold pool and will be transported within the spreading cold pool, to some extent. Complexity is then added due to new potential aerosol sources lofted by wind action at the surface, either within the cold pool itself or by lofting ahead of the cold pool and subsequent turbulent mixing within the cold pool leading edge (Seigel and van den Heever 2012). In IOP22, the first cold pool passage event (CP1, highlighted in Figs. 5a,b), which is also the coldest and deepest among the four (Table 1), produces increased > 500-nm aerosol concentrations, fluorescent particle concentrations, and INP concentrations (Figs. 4e,g). The cold pool impact is similar in character to the rainfall event of IOP22, discussed above, although with reduced magnitude. Aerosol concentrations < 500 nm increased ~10 min ahead of the cold pool boundary's passage, with some fluctuation in these concentrations during the cold pool passage period. The shallower and thermodynamically weaker CP2 (highlighted in Fig. 5c) produced similar increases in coarse aerosol, fluorescent particles, and INPs, though concentrations immediately prior to passage were increased from the preceding cold pool and rainfall events, highlighting the role played by cold pool trains on aerosol transport and ambient concentrations (Neumaier 2023). Aerosol concentrations < 500 nm were relatively stable through the CP2 passage window, though they increased dramatically after the cold pool passage (from ~2000 to ~5000 cm^{-3}) as other particle concentrations were decreasing. While fluorescent particles can sometimes be nonbiological (Pöhlker et al. 2012; Savage et al. 2017), the fluorescent particle increases during IOP22 were attributed to fungal spores by microscopy analysis (Fig. 4i; Feldman et al. 2026). High-time-resolution measurements of fluorescent and total particles (0.5–2.5 μm) demonstrated significant strong, positive correlations with INPs (<2.5 μm) during cold pools and rain (Fig. 4g; Feldman et al. 2026). Pollen concentrations were highest prior to cold pool and rainfall events, with an ~10× decrease comparing before and

after events (Fig. 4i). There was no evidence of either pollen rupture or fungal spore bursting based on lack of detection of relevant chemical tracers for fungal spores (mannitol) and pollen (sucrose and fructose) in particles with aerodynamic diameters of 0.25–1.0 μm for this event (Feldman et al. 2026). It is possible that the increase in small particles arises from a process such as transport of recently formed particles from the free troposphere, but given the simultaneous decrease in larger particles, a local dust source is unlikely. While long-range transported biomass burning aerosols were present for some BACS campaign periods, based on ECMWF forecasts (Morcrette et al. 2009) and BACS ground measurements of levoglucosan, and could be transported from the free troposphere to the surface in a similar manner, there was no evidence of significant impacts for these cases.

IOP06 provides contrasting behavior with cold pool passage. The CP3 event included a boundary emanating from precipitation to the southwest (SW) of the site (Figs. 5d,e, clearly visible on radar), followed closely by a cold pool passage from the north (Fig. 5e, annotated but not evident on radar). The CP3 event, therefore, represents a collision between two boundaries. Wind speed exhibited a decrease of ~6.5 m s^{-1}, possibly due to the boundary collision, followed by an increase of 4.5 m s^{-1} and change in wind direction to northerly in the middle of the passage period associated with the cold pool from the north (Fig. 3d; Table 1). Aerosol and fluorescent particle concentrations increased 3–5× prior to the initial CP3 passage (aerosols < 500 nm from ~2000 to ~10 000 cm^{-3}, aerosols > 500 nm from ~1 to ~3 cm^{-3}, fluorescent aerosols from ~0.2 to ~0.6 cm^{-3}) and stabilized during the passage period (Figs. 4f,h). The following cold pool passage, CP4, which coincided with light precipitation, produced no changes in any aerosol concentrations (Figs. 4f,h) despite being thermodynamically stronger than CP3 and having the largest near-surface wind speed increase among the four CPs (Table 1).

Offline INP samples collected during IOP22 (Fig. 7, left), collected before CP1, during rain/CPs, and after CP2, agree well with online INP data and reveal changes across the full temperature range. A second set of offline INP samples, segregated by size and type (Figs. S1–S3), collected for a period ~6.5 h before and ~20.5 h after first rainfall, have significantly higher INP concentrations after rainfall than before in all sizes. Precipitation water collected during IOP22, when scaled to reasonable cloud water content as discussed in Mignani et al. (2025), compare well with INP concentrations before and after rainfall, rather than the increased concentrations observed during rainfall. This suggests that the precipitation water was not significantly influenced by below-cloud scavenging of INP during the rainfall event. It also suggests that INP concentrations throughout the precipitating cloud are not greatly altered by

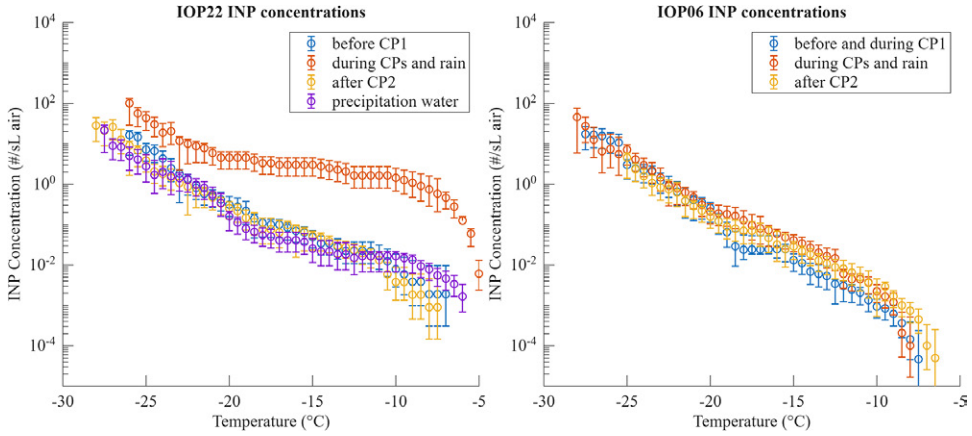

Fig. 7. INP spectra from offline samples collected during (left) IOP22 and (right) IOP06. Sample collection times for IOP22 are before rain: 1425–1512 LT, during rain: 1517–1634 LT, and after rain: 1643–1821 LT. Sample collection times for IOP06 are before rain: 0924–1404 LT, during rain: 1421–1629 LT, and after rain: 1710–2133 LT.

enhanced INP concentrations during rainfall in this case but does not rule out any influence of these enhanced concentrations on the precipitating cloud due to the complex transport and microphysical pathways that could be involved.

Comparing the total INP concentrations between these two offline sample sets for IOP22 (summed across all size-segregated samples), there is good agreement between the two sample sets before rainfall, but the postrain (20.5-h collection) sample has significantly lower INP concentrations than the offline sample collected during rainfall (2.1-h collection). Because there were no additional rainfall events recorded (Fig. S5), the difference between the collection times can be accounted for in the higher-resolution sample, and excellent agreement is produced (Fig. S6), indicating that in this case, the enhancement in the 20.5 h after first rainfall is dominantly due to INP emissions that occur in the ~2-h surrounding rainfall and cold pool events. Treatments on size-resolved offline samples reveal that the increased INP from rainfall and cold pools is almost exclusively biological in origin. There are significant contributions from <250-nm, from 250- to 1000-nm, from 1- to 2.5-μm, and from 2.5- to 10-μm size ranges but not from >10-μm aerosols. The polydisperse nature of INPs, and significant population below 250 nm, suggests either a biological source of INPs that is internally mixed with other aerosols, such from a soil source (Augustin-Bauditz et al. 2016; Suski et al. 2018), or a variety of different biological sources, although there may also be an impact of bouncing particles appearing outside their nominal size fractions (Cheng and Yeh 1979). At temperatures below –12.5°C, the 2.5–10-μm size range is dominant, which coincides with the size of many intact fungal spore species. In support of this interpretation, BACS measurements of spore concentrations and INPs evolve similarly over time. Ruptured pollen or fragmented spores cannot be ruled out as an important INP source in this case, even with their low tracer concentrations, due to the very low fraction of total aerosols acting as INP.

Offline measurements of INP concentrations in IOP06 (Fig. 7, right) divide the period of increased aerosol concentrations between the before and during precipitation periods, but neither of these samples have significantly increased INP concentrations compared to the period after precipitation with the lowest aerosol concentrations. This may be partly due to the enhanced aerosol period composing only a small portion of sample time or the increased aerosol concentrations arising from aerosol types that are poor INP sources. There is a clear simultaneous rise in aerosols and fluorescent (likely biological) aerosols before and during CP3 (Figs. 4f,h), which suggests the bioaerosols released from this event lack the efficient ice nucleating components observed during IOP22. Size-resolved INP concentrations are available only for the full 24-h period (Fig. S4), due to the light precipitation recorded at the SGRC site not triggering a rainwater sensor for a sample change at the tower location. Despite lower concentrations and little to no aerosolization due to impaction of raindrops, heat treatments reveal dominantly biological INPs across all size classes. In this sample, aerosols < 2.5 μm dominate INP concentrations at temperatures > –15°C, similar to IOP22 but with less impact from the 2.5- to 10-μm size range. Pollen concentrations (Fig. 4k) are highest for the CP3 sample period, decreasing slightly into the period of precipitation and the start of CP4 and decreasing by a factor of ~7× for the period during/after CP4 and the second precipitation event. Fungal spore concentrations (Fig. 4k) increase ~2× during precipitation compared to before and remain enhanced through CP4. The differences in aerosol response between IOP22 and IOP06 could be largely driven by the difference in precipitation intensity between the two cases, with the lighter, intermittent precipitation and virga producing less aerosol through droplet impaction and subsequently less aerosol appearing in cold pools. The differing levels of rainfall accumulation between BACS-I and BACS-II and their cascading ecological impacts may also play a role in the observed differences. The aerosol transport dynamics surrounding these convective events likely have a significant role as well, possibly through the transport

of free-tropospheric air into the boundary layer, which is difficult to quantify experimentally (De Wekker and Kossmann 2015; Jin et al. 2021).

4. Summary and future work

We have presented an overview of the BACS project and examined two case studies from the BACS-I and BACS-II field campaigns, focusing on properties of cold pools and the aerosol changes surrounding cold pool passages and rainfall events. These case studies were chosen to highlight the variability in cold pool and precipitation events observed in the campaign and the differences in aerosol responses. Some of the cold pool and precipitation events examined result in marked increases in aerosol, bioaerosol, and INP concentrations, while others leave them unperturbed or even coincide with decreased concentrations, though strong positive correlations between accumulated rainfall and INP concentrations exist within the broader dataset (Mignani et al. 2025). Some of the environmental, storm, and aerosol factors that likely play a role in these disparate responses to cold pool and precipitation events are suggested, but further investigation is needed to understand the mechanisms of aerosol and bioaerosol release, transport, and deposition within this context. An examination of INP concentrations in IOP22 reveals that event-driven INP enhancements quickly decay over the course of a few hours, but averaged concentrations (~12–24 h) remain enhanced, due primarily to this short-lived enhancement. This suggests that long-term increases in INP concentration may be driven by direct emissions from rainfall and cold-pool-associated release of biological materials, rather than rainfall leading to ecosystem-level changes or rainfall-prompted direct release of biological materials that have been suggested previously (Morris et al. 2014, 2017). It is also plausible that multiple different release mechanisms of bioaerosol and INP during or following rainfall are important, with different mechanisms dominating in different locations or even cases. Further investigations using this comprehensive campaign dataset are encouraged, with access online (https://www.eol.ucar.edu/field_projects/bacs).

Experimental observations from the BACS campaign have motivated modeling studies examining the behavior of cold pool trains and how multiple cold pools passing through a region impact the transport of background and newly generated aerosols (Neumaier 2023; Neumaier et al. 2026, manuscript submitted to *J. Atmos. Sci.*), as well as how rain-released bioaerosols can be transported through different types of convective storms (Davis et al. 2025). Additional studies are being conducted on cold pool and aerosol processes using the wealth of data collected during this campaign, including development of a database of cold pool passages and their associated properties. Radiosonde, drone, and surface observations are being used to investigate the relationships among cold pool properties, their vertical structure, and the intensity of the parent convection and layers of increased aerosol concentrations aloft within cold pools (Heffernan 2024). The in-depth analysis of observations of bioaerosols, bioaerosol tracers, and INP changes due to rainfall and cold pool events is being conducted across the many case studies available to elucidate trends in bacteria, fungal spore, and pollen responses to CPs and precipitation (Feldman et al. 2026). Motivated by observed long-lasting enhanced INPs during/following rainfall and cold pool events, the investigation of correlation between regional rainfall parameters, transport, and observed INP concentrations is underway. An analysis of bioaerosol wet deposition is also ongoing, examining the relative roles of in-cloud and below-cloud scavenging. Sequenced airborne DNA measurements are being leveraged to examine the evolution of airborne microbial communities in the context of the breadth of other observations discussed. Drawing on the extensive dataset created during this project, we look forward to uncovering the potentially exciting relationships between aerosols, rainfall, and cold pools these observations hold.

Acknowledgments. We would like to acknowledge support for this project from the U.S. Department of Agriculture Agency of Agricultural Research Services by providing site access at the Central Plains Experimental Range. The National Ecological Observatory Network is a program sponsored by the National Science Foundation and operated under cooperative agreement by Battelle. This material is based in part upon work supported by the National Science Foundation through the NEON Program. Data collected/used in this research were obtained through the NEON Assignable Assets program. Special thanks to Amy Bibbey and Troy Bauder and other staff at the Colorado Agricultural Experiment Station for help in supporting and scheduling facilities at the Semi-Arid Grasslands Research Center. We thank Russ Schumacher and Peter Goble at the Colorado Climate Center for creation of precipitation maps during field campaign periods (Fig. 1). Support for the BACS campaigns was provided by NSF AGS-2105938 and AGS-2106370. We gratefully acknowledge support for BROADN from the NSF Biology Integration Institutes Program under Award 2120117. We thank the CSU One Health Institute for contributions to and support of BROADN research. C. Mignani acknowledges the Swiss National Science Foundation for the Postdoc Mobility Grant P500PN_206661.

Data availability statement. Data for this article are available at the National Center for Atmospheric Research Earth Observatory Laboratory Field Data Archive through https://www.eol.ucar.edu/field_projects/bacs. NEON data are available through the NEON data portal at https://data.neonscience.org/data-products/explore.

References

Augustine, D., A. Davidson, K. Dickinson, and B. Van Pelt, 2021: Thinking like a grassland: Challenges and opportunities for biodiversity conservation in the Great Plains of North America. *Rangeland Ecol. Manage.*, **78**, 281–295, https://doi.org/10.1016/j.rama.2019.09.001.

Augustine, D. J., and Coauthors, 2024: The LTAR grazing land common experiment at the Central Plains Experimental Range: Collaborative adaptive rangeland management. *J. Environ. Qual.*, **53**, 904–912, https://doi.org/10.1002/jeq2.20599.

Augustin-Bauditz, S., H. Wex, C. Denjean, S. Hartmann, J. Schneider, S. Schmidt, M. Ebert, and F. Stratmann, 2016: Laboratory-generated mixtures of mineral dust particles with biological substances: Characterization of the particle mixing state and immersion freezing behavior. *Atmos. Chem. Phys.*, **16**, 5531–5543, https://doi.org/10.5194/acp-16-5531-2016.

Benjamin, T. B., 1968: Gravity currents and related phenomena. *J. Fluid Mech.*, **31**, 209–248, https://doi.org/10.1017/S0022112068000133.

Bukowski, J., and S. C. van den Heever, 2022: The impact of land surface properties on haboobs and dust lofting. *J. Atmos. Sci.*, **79**, 3195–3218, https://doi.org/10.1175/JAS-D-22-0001.1.

Charba, J., 1974: Application of gravity current model to analysis of squall-line gust front. *Mon. Wea. Rev.*, **102**, 140–156, https://doi.org/10.1175/1520-0493(1974)102<0140:AOGCMT>2.0.CO;2.

Cheng, I., A. Al Mamun, and L. Zhang, 2021: A synthesis review on atmospheric wet deposition of particulate elements: Scavenging ratios, solubility, and flux measurements. *Environ. Rev.*, **29**, 340–353, https://doi.org/10.1139/er-2020-0118.

Cheng, Y.-S., and H.-C. Yeh, 1979: Particle bounce in cascade impactors. *Environ. Sci. Technol.*, **13**, 1392–1396, https://doi.org/10.1021/es60159a017.

Conen, F., C. E. Morris, J. Leifeld, M. V. Yakutin, and C. Alewell, 2011: Biological residues define the ice nucleation properties of soil dust. *Atmos. Chem. Phys.*, **11**, 9643–9648, https://doi.org/10.5194/acp-11-9643-2011.

Daly, C., G. H. Taylor, W. P. Gibson, T. W. Parzybok, G. L. Johnson, and P. A. Pasteris, 2000: High-quality spatial climate data sets for the United States and beyond. *Trans. ASAE*, **43**, 1957–1962, https://doi.org/10.13031/2013.3101.

D'Amato, G., and Coauthors, 2016: Thunderstorm-related asthma: What happens and why. *Clin. Exp. Allergy*, **46**, 390–396, https://doi.org/10.1111/cea.12709.

Davis, C. M., S. C. van den Heever, L. D. Grant, S. M. Kreidenweis, C. Mignani, R. J. Perkins, and E. A. Stone, 2025: The entrainment of air from rainy surface regions and its implications for bioaerosol transport in three deep convective storm morphologies. EGUsphere, https://doi.org/10.5194/egusphere-2025-2968.

De Wekker, S. F. J., and M. Kossmann, 2015: Convective boundary layer heights over mountainous terrain—A review of concepts. *Front. Earth Sci.*, **3**, 77, https://doi.org/10.3389/feart.2015.00077.

Dickerson, R. R., and Coauthors, 1987: Thunderstorms: An important mechanism in the transport of air pollutants. *Science*, **235**, 460–465, https://doi.org/10.1126/science.235.4787.460.

Droegemeier, K. K., and R. B. Wilhelmson, 1985a: Three-dimensional numerical modeling of convection produced by interacting thunderstorm outflows. Part I: Control simulation and low-level moisture variations. *J. Atmos. Sci.*, **42**, 2381–2403, https://doi.org/10.1175/1520-0469(1985)042<2381:TDNMOC>2.0.CO;2.

——, and ——, 1985b: Three-dimensional numerical modeling of convection produced by interacting thunderstorm outflows. Part II: Variations in vertical wind shear. *J. Atmos. Sci.*, **42**, 2404–2414, https://doi.org/10.1175/1520-0469(1985)042<2404:TDNMOC>2.0.CO;2.

Duce, R. A., and Coauthors, 1991: The atmospheric input of trace species to the world ocean. *Global Biogeochem. Cycles*, **5**, 193–259, https://doi.org/10.1029/91GB01778.

Elbert, W., P. E. Taylor, M. O. Andreae, and U. Pöschl, 2007: Contribution of fungi to primary biogenic aerosols in the atmosphere: Wet and dry discharged spores, carbohydrates, and inorganic ions. *Atmos. Chem. Phys.*, **7**, 4569–4588, https://doi.org/10.5194/acp-7-4569-2007.

Engerer, N. A., D. J. Stensrud, and M. C. Coniglio, 2008: Surface characteristics of observed cold pools. *Mon. Wea. Rev.*, **136**, 4839–4849, https://doi.org/10.1175/2008MWR2528.1.

Falk, N. M., and S. C. van den Heever, 2023: Environmental modulation of mechanical and thermodynamic forcing from cold pool collisions. *J. Atmos. Sci.*, **80**, 375–395, https://doi.org/10.1175/JAS-D-22-0020.1.

——, and Coauthors, 2025: Do cold pools propagate according to theory? *J. Atmos. Sci.*, **82**, 1481–1497, https://doi.org/10.1175/JAS-D-24-0136.1.

Feldman, T. K., and Coauthors, 2026: Convective storms alter bioaerosol populations through cold pools and precipitation. *Environ. Sci. Atmos.*, **6**, 286–309, https://doi.org/10.1039/d5ea00129c.

Fernando, J., and Coauthors, 2025: BACS: Rainwater measurements, version 1.0. NSF NCAR Earth Observing Laboratory, accessed 14 November 2025, https://doi.org/10.26023/KQ4G-CCYG-ZS0Y.

Field, P. R., and Coauthors, 2017: Secondary ice production: Current state of the science and recommendations for the future. *Ice Formation and Evolution in Clouds and Precipitation: Measurement and Modeling Challenges*, *Meteor. Monogr.*, No. 58, Amer. Meteor. Soc., https://doi.org/10.1175/AMSMONOGRAPHS-D-16-0014.1.

Fröhlich-Nowoisky, J., T. C. J. Hill, B. G. Pummer, P. Yordanova, G. D. Franc, and U. Pöschl, 2015: Ice nucleation activity in the widespread soil fungus *Mortierella alpina*. *Biogeosciences*, **12**, 1057–1071, https://doi.org/10.5194/bg-12-1057-2015.

——, and Coauthors, 2016: Bioaerosols in the Earth system: Climate, health, and ecosystem interactions. *Atmos. Res.*, **182**, 346–376, https://doi.org/10.1016/j.atmosres.2016.07.018.

Gosselin, M. I., and Coauthors, 2016: Fluorescent bioaerosol particle, molecular tracer, and fungal spore concentrations during dry and rainy periods in a semi-arid forest. *Atmos. Chem. Phys.*, **16**, 15165–15184, https://doi.org/10.5194/acp-16-15165-2016.

Grant, L. D., and S. C. van den Heever, 2016: Cold pool dissipation. *J. Geophys. Res. Atmos.*, **121**, 1138–1155, https://doi.org/10.1002/2015JD023813.

——, and ——, 2018: Cold pool-land surface interactions in a dry continental environment. *J. Adv. Model. Earth Syst.*, **10**, 1513–1526, https://doi.org/10.1029/2018MS001323.

——, T. P. Lane, and S. C. van den Heever, 2018: The role of cold pools in tropical oceanic convective systems. *J. Atmos. Sci.*, **75**, 2615–2634, https://doi.org/10.1175/JAS-D-17-0352.1.

——, B. Kirsch, J. Bukowski, N. M. Falk, C. A. Neumaier, M. Sakradzija, S. C. van den Heever, and F. Ament, 2024: How variable are cold pools? *Geophys. Res. Lett.*, **51**, e2023GL106784, https://doi.org/10.1029/2023GL106784.

Grant, L., S. W. Freeman, G. R. Leung, P. J. DeMott, S. Kreidenweis, S. C. van den Heever, E. A. Stone, and R. J. Perkins, 2026. BACS: IOP summaries and IOP radar animations. Version 1.0. NSF NCAR Earth Observing Laboratory, accessed 18 June 2026, https://doi.org/10.26023/WZTV-W6KZ-DM0A.

Harun, N.-S., P. Lachapelle, and J. Douglass, 2019: Thunderstorm-triggered asthma: What we know so far. *J. Asthma Allergy*, **12**, 101–108, https://doi.org/10.2147/JAA.S175155.

Hazlett, D. L., 1998: Vascular plant species of the Pawnee National Grassland. United States Department of Agriculture, Forest Service, Rocky Mountain Research Station Tech. Rep. RMRS-GTR-17, 26 pp.

Heffernan, B., 2024: Measurement of low-altitude aerosol layers surrounding convective cold pool passage observed by uncrewed aircraft. Colorado State University, accessed 24 November 2025, https://hdl.handle.net/10217/239128.

Hirst, J. M., and O. J. Stedman, 1963: Dry liberation of fungus spores by raindrops. *J. Gen. Microbiol.*, **33**, 335–344, https://doi.org/10.1099/00221287-33-2-335.

Hofer, S., and Coauthors, 2024: Realistic representation of mixed-phase clouds increases projected climate warming. *Commun. Earth Environ.*, **5**, 390, https://doi.org/10.1038/s43247-024-01524-2.

Hoose, C., and O. Möhler, 2012: Heterogeneous ice nucleation on atmospheric aerosols: A review of results from laboratory experiments. *Atmos. Chem. Phys.*, **12**, 9817–9854, https://doi.org/10.5194/acp-12-9817-2012.

Huffman, J. A., and Coauthors, 2013: High concentrations of biological aerosol particles and ice nuclei during and after rain. *Atmos. Chem. Phys.*, **13**, 6151–6164, https://doi.org/10.5194/acp-13-6151-2013.

Hughes, D. D., C. B. A. Mampage, L. M. Jones, Z. Liu, and E. A. Stone, 2020: Characterization of atmospheric pollen fragments during springtime thunderstorms. *Environ. Sci. Technol. Lett.*, **7**, 409–414, https://doi.org/10.1021/acs.estlett.0c00213.

Jaenicke, R., 2005: Abundance of cellular material and proteins in the atmosphere. *Science*, **308**, 73–73, https://doi.org/10.1126/science.1106335.

Janssen, R. H. H., C. L. Heald, A. L. Steiner, A. E. Perring, J. A. Huffman, E. S. Robinson, C. H. Twohy, and L. D. Ziemba, 2021: Drivers of the fungal spore bioaerosol budget: Observational analysis and global modeling. *Atmos. Chem. Phys.*, **21**, 4381–4401, https://doi.org/10.5194/acp-21-4381-2021.

Jin, X., X. Cai, Q. Huang, X. Wang, Y. Song, and T. Zhu, 2021: Atmospheric boundary layer—Free troposphere air exchange in the North China Plain and its impact on $PM_{2.5}$ pollution. *J. Geophys. Res. Atmos.*, **126**, e2021JD034641, https://doi.org/10.1029/2021JD034641.

Joung, Y. S., Z. Ge, and C. R. Buie, 2017: Bioaerosol generation by raindrops on soil. *Nat. Commun.*, **8**, 14668, https://doi.org/10.1038/ncomms14668.

Kanji, Z. A., L. A. Ladino, H. Wex, Y. Boose, M. Burkert-Kohn, D. J. Cziczo, and M. Krämer, 2017: Overview of ice nucleating particles. *Ice Formation and Evolution in Clouds and Precipitation: Measurement and Modeling Challenges*, *Meteor. Monogr.*, 58, Amer. Meteor. Soc., https://doi.org/10.1175/AMSMONOGRAPHS-D-16-0006.1.

Korolev, A., and T. Leisner, 2020: Review of experimental studies of secondary ice production. *Atmos. Chem. Phys.*, **20**, 11 767–11 797, https://doi.org/10.5194/acp-20-11767-2020.

Krauss, R., C. Meier, M. Patterson, and O. Smith, 2018: Terrestrial Observation System (TOS) site characterization report: Domain 10. National Ecological Observatory Network, 63 pp., https://data.neonscience.org/api/v0/documents/NEON.DOC.003883vB.

Lohmann, U., and D. Neubauer, 2018: The importance of mixed-phase and ice clouds for climate sensitivity in the global aerosol–climate model ECHAM6-HAM2. *Atmos. Chem. Phys.*, **18**, 8807–8828, https://doi.org/10.5194/acp-18-8807-2018.

Markowski, P., and Y. Richardson, 2010: *Mesoscale Meteorology in Midlatitudes.* John Wiley and Sons, 407 pp., https://doi.org/10.1002/9780470682104.

Meyer, B., and J. O. Haerter, 2020: Mechanical forcing of convection by cold pools: Collisions and energy scaling. *J. Adv. Model. Earth Syst.*, **12**, e2020MS002281, https://doi.org/10.1029/2020MS002281.

Mignani, C., and Coauthors, 2025: Ice-nucleating particles are emitted by raindrop impact. *J. Geophys. Res. Atmos.*, **130**, e2024JD042584, https://doi.org/10.1029/2024JD042584.

Miller, S. D., A. P. Kuciauskas, M. Liu, Q. Ji, J. S. Reid, D. W. Breed, A. L. Walker, and A. Al Mandoos, 2008: Haboob dust storms of the southern Arabian Peninsula. *J. Geophys. Res.*, **113**, D01202, https://doi.org/10.1029/2007JD008550.

Morcrette, J.-J., and Coauthors, 2009: Aerosol analysis and forecast in the European Centre for Medium-Range Weather Forecasts Integrated Forecast System: Forward modeling. *J. Geophys. Res.*, **114**, D06206, https://doi.org/10.1029/2008JD011235.

Morris, C. E., F. Conen, J. Alex Huffman, V. Phillips, U. Pöschl, and D. C. Sands, 2014: Bioprecipitation: A feedback cycle linking earth history, ecosystem dynamics and land use through biological ice nucleators in the atmosphere. *Global Change Biol.*, **20**, 341–351, https://doi.org/10.1111/gcb.12447.

——, S. Soubeyrand, E. K. Bigg, J. M. Creamean, and D. C. Sands, 2017: Mapping rainfall feedback to reveal the potential sensitivity of precipitation to biological aerosols. *Bull. Amer. Meteor. Soc.*, **98**, 1109–1118, https://doi.org/10.1175/BAMS-D-15-00293.1.

Morrison, H., and Coauthors, 2020: Confronting the challenge of modeling cloud and precipitation microphysics. *J. Adv. Model. Earth Syst.*, **12**, e2019MS001689, https://doi.org/10.1029/2019MS001689.

NEON, 2025a: Phenology images (DP1.00033.001). NEON, accessed 20 November 2025, https://data.neonscience.org/data-products/DP1.00033.001.

——, 2025b: Bundled data products - Eddy covariance (DP4.00200.001). National Ecological Observatory Network, accessed 20 November 2025, https://doi.org/10.48443/R7ZP-Y487.

Neumaier, C. A., 2023: Cold pool train dynamics and transport. Colorado State University, accessed 14 November 2025, https://hdl.handle.net/10217/237345.

O'Sullivan, D., B. J. Murray, J. F. Ross, and M. E. Webb, 2016: The adsorption of fungal ice-nucleating proteins on mineral dusts: A terrestrial reservoir of atmospheric ice-nucleating particles. *Atmos. Chem. Phys.*, **16**, 7879–7887, https://doi.org/10.5194/acp-16-7879-2016.

Pereira Freitas, G., K. Adachi, F. Conen, D. Heslin-Rees, R. Krejci, Y. Tobo, K. E. Yttri, and P. Zieger, 2023: Regionally sourced bioaerosols drive high-temperature ice nucleating particles in the Arctic. *Nat. Commun.*, **14**, 5997, https://doi.org/10.1038/s41467-023-41696-7.

Pöhlker, C., J. A. Huffman, and U. Pöschl, 2012: Autofluorescence of atmospheric bioaerosols—Fluorescent biomolecules and potential interferences. *Atmos. Meas. Tech.*, **5**, 37–71, https://doi.org/10.5194/amt-5-37-2012.

PRISM Group, 2023: PRISM Weather Data. Oregon State University, accessed 1 June 2025, https://prism.oregonstate.edu.

Provod, M., J. H. Marsham, D. J. Parker, and C. E. Birch, 2016: A characterization of cold pools in the West African Sahel. *Mon. Wea. Rev.*, **144**, 1923–1934, https://doi.org/10.1175/MWR-D-15-0023.1.

Purdom, J. F. W., 1976: Some uses of high-resolution GOES imagery in the mesoscale forecasting of convection and its behavior. *Mon. Wea. Rev.*, **104**, 1474–1483, https://doi.org/10.1175/1520-0493(1976)104<1474:SUOHRG>2.0.CO;2.

Rotunno, R., J. B. Klemp, and M. L. Weisman, 1988: A theory for strong, long-lived squall lines. *J. Atmos. Sci.*, **45**, 463–485, https://doi.org/10.1175/1520-0469(1988)045<0463:ATFSLL>2.0.CO;2.

Savage, N. J., C. E. Krentz, T. Könemann, T. T. Han, G. Mainelis, C. Pöhlker, and J. A. Huffman, 2017: Systematic characterization and fluorescence threshold strategies for the wideband integrated bioaerosol sensor (WIBS) using size-resolved biological and interfering particles. *Atmos. Meas. Tech.*, **10**, 4279–4302, https://doi.org/10.5194/amt-10-4279-2017.

Seigel, R. B., and S. C. van den Heever, 2012: Dust lofting and ingestion by supercell storms. *J. Atmos. Sci.*, **69**, 1453–1473, https://doi.org/10.1175/JAS-D-11-0222.1.

Steinert, A., 2016: NEON site-level plot summary Central Plains Experimental Range (CPER). USDA, 5 pp., https://data.neonscience.org/api/v0/documents/CPER_Soil_SiteSummary.

Subba, T., Y. Zhang, and A. L. Steiner, 2023: Simulating the transport and rupture of pollen in the atmosphere. *J. Adv. Model. Earth Syst.*, **15**, e2022MS003329, https://doi.org/10.1029/2022MS003329.

Suphioglu, C., M. B. Singh, P. Taylor, R. Bellomo, P. Holmes, R. Puy, and R. B. Knox, 1992: Mechanism of grass-pollen-induced asthma. *Lancet*, **339**, 569–572, https://doi.org/10.1016/0140-6736(92)90864-y.

Suski, K. J., T. C. J. Hill, E. J. T. Levin, A. Miller, P. J. DeMott, and S. M. Kreidenweis, 2018: Agricultural harvesting emissions of ice-nucleating particles. *Atmos. Chem. Phys.*, **18**, 13 755–13 771, https://doi.org/10.5194/acp-18-13755-2018.

Taylor, P. E., R. C. Flagan, R. Valenta, and M. M. Glovsky, 2002: Release of allergens as respirable aerosols: A link between grass pollen and asthma. *J. Allergy Clin. Immunol.*, **109**, 51–56, https://doi.org/10.1067/mai.2002.120759.

Testa, B., and Coauthors, 2021: Ice nucleating particle connections to regional Argentinian land surface emissions and weather during the cloud, aerosol, and complex terrain interactions experiment. *J. Geophys. Res. Atmos.*, **126**, e2021JD035186, https://doi.org/10.1029/2021JD035186.

Thorpe, A. J., M. J. Miller, and M. W. Moncrieff, 1982: Two-dimensional convection in non-constant shear: A model of mid-latitude squall lines. *Quart. J. Roy. Meteor. Soc.*, **108**, 739–762, https://doi.org/10.1002/qj.49710845802.

van den Heever, S. C., and Coauthors, 2021: The Colorado State University Convective CLoud Outflows and UpDrafts Experiment (C^3LOUD-Ex). *Bull. Amer. Meteor. Soc.*, **102**, E1283–E1305, https://doi.org/10.1175/BAMS-D-19-0013.1.

Weisman, M. L., and R. Rotunno, 2004: "A theory for strong long-lived squall lines" revisited. *J. Atmos. Sci.*, **61**, 361–382, https://doi.org/10.1175/1520-0469(2004)061<0361:ATFSLS>2.0.CO;2.

Werchner, S., E. Gute, C. Hoose, C. Kottmeier, A. Pauling, H. Vogel, and B. Vogel, 2022: When do subpollen particles become relevant for ice nucleation processes in clouds? *J. Geophys. Res. Atmos.*, **127**, e2021JD036340, https://doi.org/10.1029/2021JD036340.

Wozniak, M. C., F. Solmon, and A. L. Steiner, 2018: Pollen rupture and its impact on precipitation in clean continental conditions. *Geophys. Res. Lett.*, **45**, 7156–7164, https://doi.org/10.1029/2018GL077692.

Yue, S., H. Ren, S. Fan, Y. Sun, Z. Wang, and P. Fu, 2016: Springtime precipitation effects on the abundance of fluorescent biological aerosol particles and HULIS in Beijing. *Sci. Rep.*, **6**, 29618, https://doi.org/10.1038/srep29618.

Zawadowicz, M. A., K. D. Froyd, A. E. Perring, D. M. Murphy, D. V. Spracklen, C. L. Heald, P. R. Buseck, and D. J. Cziczo, 2019: Model-measurement consistency and limits of bioaerosol abundance over the continental United States. *Atmos. Chem. Phys.*, **19**, 13 859–13 870, https://doi.org/10.5194/acp-19-13859-2019.

Zhang, J., and Coauthors, 2016: Multi-Radar Multi-Sensor (MRMS) quantitative precipitation estimation: Initial operating capabilities. *Bull. Amer. Meteor. Soc.*, **97**, 621–638, https://doi.org/10.1175/BAMS-D-14-00174.1.